Volume 1 | Number 1 | Jan 2013 | Pages 1–100

Journal of
Materials Chemistry A

Materials for energy and sustainability
www.rsc.org/materialsA

ROYAL SOCIETY OF CHEMISTRY

www.rsc.org/materialsA

Functional Tuning of A-D-A Oligothiophenes: The Effect of Solvent Vapor Annealing on Blend Morphology and Solar Cell Performance

Gisela L. Schulz,[†] Mirjam Löbert,[†] Ibrahim Ata,[†] Marta Urdanpilleta,[‡] Mika Lindén,[§] Amaresh Mishra,[†]* and Peter Bäuerle[†]*

[†]Institute of Organic Chemistry II and Advanced Materials, University of Ulm, Albert-Einstein-Allee 11, D-89081 Ulm, Germany, E-mail: amaresh.mishra@uni-ulm.de, peter.baeuerle@uni-ulm.de

[‡]Department of Applied Physics I, University of the Basque Country (UPV/EHU), Plaza de Europa, 1, 20018 Donostia - San Sebastián, Spain

[§]Institute of Inorganic Chemistry II, Ulm University, Albert-Einstein-Allee 11, 89081 Ulm, Germany

Keywords: Conjugated oligomers, solution processing, bulk-heterojunction solar cells, solvent vapor annealing, morphology

Abstract

A series of solution-processable acceptor-donor-acceptor (A-D-A) oligomers consisting of various central conjugated units, namely, carbazole, benzo[2,1-*b*:3,4-*b*']dithiophene, 2,2'-bithiophene, dithieno[3,2-*b*:2',3'-*d*]silole and dithieno[3,2-*b*:2',3'-*d*]pyrrole were synthesized and developed for application in bulk-heterojunction solar cells (BHJSC). The alteration of the core moiety, while maintaining the shape of the molecular structure, enables fine-tuning of

Journal of Materials Chemistry A Accepted Manuscript

the optical energy gap and highest occupied molecular orbital (HOMO) level of the molecules. Depending on the donor strength of the core, the maximum absorption wavelength of the oligomers ranged from 488 nm to 560 nm in solution and from 530 nm to 694 nm in neat films. HOMO energy levels were shifted in a stepwise fashion from -5.8 to -5.3 eV yielding oligomers with HOMO-LUMO energy gap between 2.04 and 1.60 eV. The structural fine-tuning is further visible in the photovoltaic performance. BHJ solar cells prepared using these oligomers as donor and [6,6]-phenyl-C_{61}-butyric acid methyl ester ($PC_{61}BM$) as acceptor demonstrated power conversion efficiencies between 1.4 and 5.9% after solvent vapor annealing. Exposure of the photoactive layer to organic solvent vapor led to re-organization of the donor material within the blend and a large enhancement of J_{SC} and FF was observed. The role of solvent vapor annealing on the degree of crystallinity and blend morphology was further investigated by grazing incident X-ray diffraction (GIXRD) and atomic force microscopy (AFM) analysis.

Introduction

Since the first reports on efficient bulk-heterojunction solar cells (BHJSC) with PCEs >4% using solution-processable small molecular materials in 2009,[1] the field has been expanding rapidly as a competitive alternative to the widely used polymeric donor materials.[2-5] A wide range of materials classes have been investigated in oligomer solar cells including: squarines,[6] merocyanines,[7, 8] triphenylamine,[9-13] a variety of functional oligothiophenes comprising 2,5-diketopyrrolo[3,4-c]pyrrole,[14-17] dithieno[3,2-b:2',3'-d]silole,[18-20] dithieno[3,2-b:2',3'-d]pyrrole,[21, 22] or benzo[1,2-b:4,5-b']dithiophenes[23, 24] moieties. Various synthetic strategies have been developed to prepare these conjugated molecular materials with donor-acceptor (D-A) structure allowing them to effectively tune the optical properties and energy levels by choosing appropriate D and A blocks.[24-26] In comparison to conjugated polymers,[27-29] prepara-

tion of these small molecular or (co)oligomeric donors sometimes requires multi-step synthetic approaches, however, they offer a well-defined structure without end-group contamination, high purity, high charge carrier mobility, and good batch-to-batch reproducibility.[25, 30-32] Very recently, with suitable molecular design, new device architectures, and optimization of the processing techniques impressive power conversion efficiencies (PCE) of over 9% have been achieved in single junction small molecule-based BHJSCs.[33-35] The photoactive layer in BHJSCs is composed of a nanoscale bicontinuous interpenetrating network of molecular donor and fullerene derivatives as electron acceptor to facilitate efficient charge separation and extraction. In these devices, the absorbed incident photons generate tightly bound electron–hole pairs, which then dissociate into free charge carriers at the D/A interface and are transported to the respective electrodes.

Indeed, the field of solution-processed BHJSCs using molecular donor has shown a great progress with respect to the molecular design and device optimization. In order to develop efficient molecular donor materials, there are many possibilities to tune the molecular structures by changing the key components, such as, D/A units, π-conjugated bridges, heteroatom substitutions, or alkyl side chains. These molecular donors allow reliable analyses of structure-properties relationships, which are a major benefit for the design of new materials. Chen and coworkers have reported A-D-A structures containing rhodanine-terminated oligothiophenes or benzo[1,2-*b*:4,5-*b*']dithiophenes generating impressive PCEs of up to 9.95% in combination with $PC_{71}BM$ as acceptor.[34, 36] Using a similar structure comprising a benzo[1,2-*b*:4,5-*b*']dithiophene central unit, Sun *et al.* reported a PCE of 9.3%.[35] In both cases, solvent vapor annealing (SVA) and thermal annealing was used to improve the device performance. On the other hand, Bazan, Heeger and co-workers have reported PCEs of 9% on a D-A-D'-A-D molecule containing a dithieno[3,2-*b*:2',3'-*d*]silole central unit flanked by two fluorinated benzothiadiazole acceptor moieties.[4, 33, 37] By systematic variation of the

acceptor blocks in a series of donor molecules, PCEs up to 6.5% have been achieved showing the significance of molecular design principle.[38] Yang and co-workers have reported a series of oligomers by varying the heteroatoms (O, S, Se) in the terminal units which showed a clear increase in PCE from 3.2-6.2% by going from furan to thiophene to selenophene.[39] Min *et al*. investigated the influence of the length of the alkyl chains (methyl, ethyl, hexyl, and dodecyl) attached to dicyanovinyl acceptor units in a series of star-shaped D-π-A molecules. Among them, the methyl-substituted derivative reached the highest PCE of 4.8% indicating that the insertion of methyl group instead of longer alkyl chain may reduce steric hindrance of the molecule and thereby enhance the intermolecular interactions, charge separation, charge carrier lifetime and consequently improve the photovoltaic performances.[11] In another instance, it has been demonstrated that the length of oligothiophene π-bridge have significant impact on the solid-state properties and photovoltaic performance within a series of star-shaped D-A molecules.[12] Recently, we have shown that the location and length of the alkyl chains in a series of dithieno[3,2-*b*:2',3'-*d*]pyrrole-based A-D-A-type oligothiophenes have strong influence on the blend morphology and consequently on the photovoltaic performance whereby PCEs higher than 6% have been achieved using SVA approach.[21]

Over the years, multiple techniques for example, choice of deposition solvent,[40, 41] thermal annealing,[42-45] SVA,[21, 36, 46-50] as well as the use of solvent additives[51-55] have emerged as efficient methods to control or influence the active layer morphology. Specifically, it has been shown that for both oligomers and polymers the SVA process can influence the D:A BHJ phase separation as well as the crystallinity of the blends leading to efficient exciton dissociation and charge extraction.

The motivation for the work presented here came from the promising solar cell performance of our dithieno[3,2-*b*:2',3'-*d*]pyrrole-based oligomers, which resulted in good PCEs (≤6.1%) and particularly very high fill factors of 72% for oligomer **5** (Figure 1).[21]

Therefore, we extended this series of A-D-A oligothiophenes to oligomers **1-4** by replacing the central dithieno[3,2-*b*:2',3'-*d*]pyrrole unit in oligomer **5** by other conjugated cores of varying donor strength as shown in Figure 1. The influence of the central bridging unit on the tuning of the frontier orbital energies, optoelectronic and photovoltaic properties were investigated. We further examine the effect of SVA on solar cell performance which involves exposing the active layer to organic vapors, like chloroform or tetrahydrofuran. The changes in the photoactive layer were followed by UV-vis absorption spectroscopy, atomic force microscopy, and grazing-incident X-ray diffraction and further correlate to the solar cell performance.
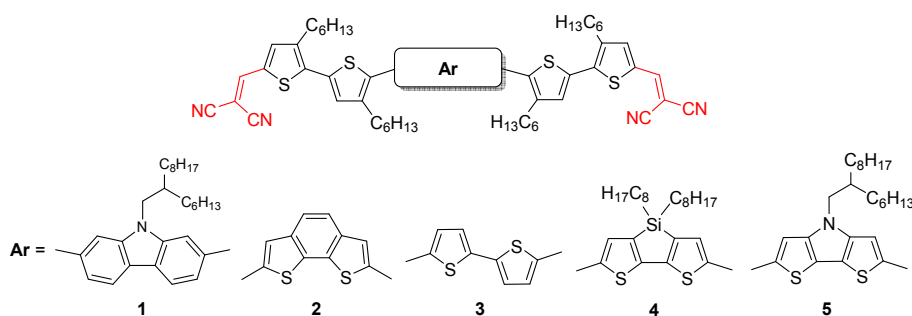
Figure 1. Chemical structures of oligomer series (**1-5**) containing different central building blocks.

Results and Discussion

The synthesis of dithieno[3,2-*b*:2',3'-*d*]pyrrole-containing A-D-A oligothiophene **5** was reported earlier.[21] By replacing the dithieno[3,2-*b*:2',3'-*d*]pyrrole central unit of **5** with conjugated moieties of weaker donor strengths, A-D-A oligomers **1-4** were synthesized as presented in Scheme 1. Oligomer **1** was prepared in 40% yield in one step by Suzuki cross-coupling reaction of carbazole diboronic ester **5** and bromo bithiophene **9** followed by Knoevenagel condensation of the resulting dicarbaldehyde with malononitrile and ammonium acetate as base. The oligomers **2-4** were synthesized by Pd[0]-catalyzed Stille cross-coupling

reactions of the respective distannylated derivatives **6-8** and DCV-capped bithiophene **10** in yields of 78 -94%.
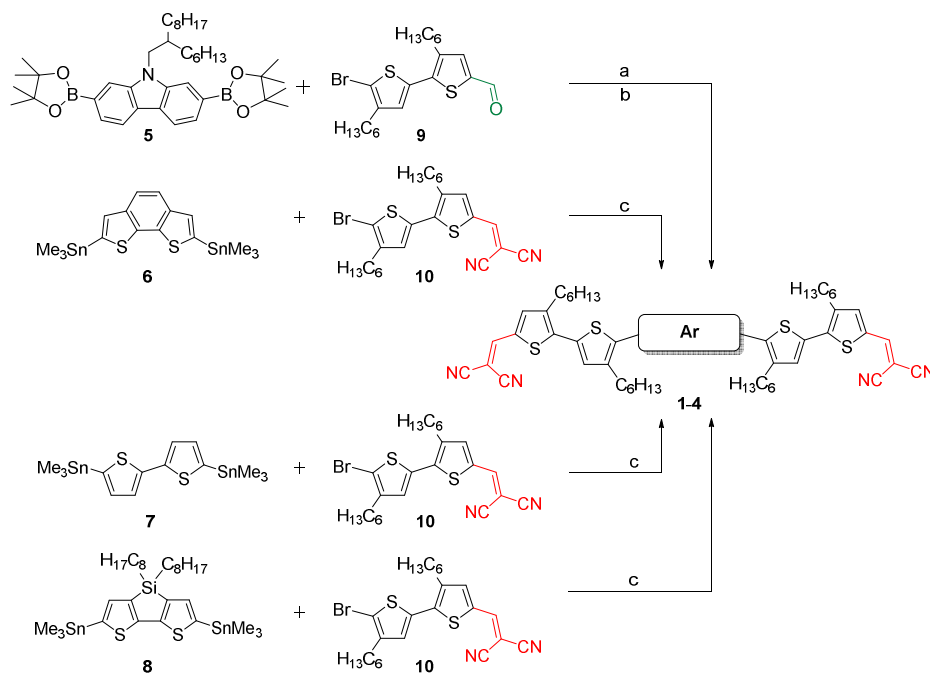
Scheme 1. Synthetic route used to oligomers **1-4**. (a) Pd$_2$dba$_3$/P(o-Tol)$_3$, Bu$_4$NOH, toluene, (b) malonitrile, NH$_4$OAc, DCE/EtOH, 40% yield, (c) Pd(PPh$_3$)$_4$, DMF, 78-94% yield.

In comparison to the dithieno[3,2-*b*:2',3'-*d*]pyrrole-based oligomer **5**, the structural modifications led to significant changes in the optical properties of the new oligomers **1-4** which were investigated by UV-vis spectroscopy on solutions and thin films. The absorption profiles of oligomers **1-5** measured in dichloromethane are shown in Figure 2a and the data are summarized in Table 1. Oligomer **5** comprising the strongest electron-donating dithieno[3,2-*b*:2',3'-*d*]pyrrole-unit showed a relatively broad band with the most red-shifted absorption maximum in the series at 560 nm and a second intensive band at 400 nm which is assign to a charge-transfer transition and to the absorption of the DCV-bithiophene subunit, respectively. Going through the series further to dithieno[3,2-*b*:2',3'-*d*]silole **4**, to bithiophene **3**, to benzo[2,1-*b*:3,4-*b*']dithiophene **2**, and finally to carbazole-derivative **1** with decreasing

donor strength, the absorption bands become narrower and the maxima successively blue-shifted to 552, 519, 500, and 488 nm, respectively. The absorption spectra of thin films are significantly red-shifted (up to 135 nm) and broadened compared to the solution spectra (Figure 2b). Within the series **1-5**, λ_{max} ranges from 530 to 653 nm with increasing donor strength of the central units. Following the observed trend the optical gaps (ΔE_{opt}) of oligomers **1-5** also decreased from 2.04 to 1.60 eV, which was calculated from the onset of the absorption band in neat films.
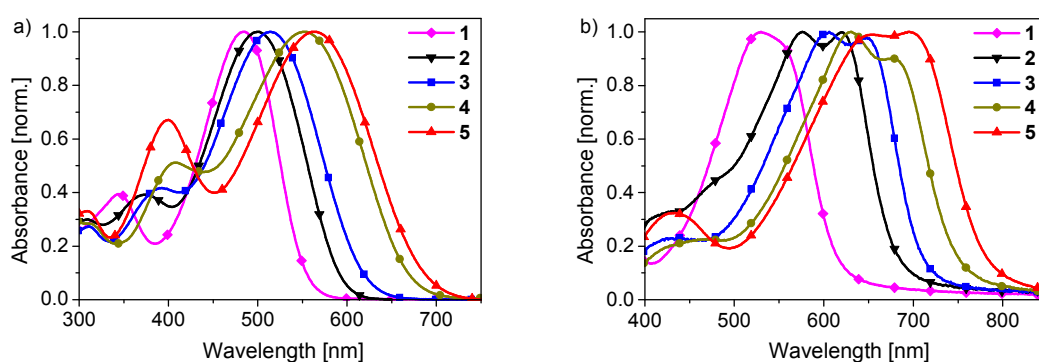
Figure 2. Absorption spectra of the series of oligomers **1–5** (a) measured in dichloromethane and (b) of thin films spin-coated from chloroform.

Table 1. Optical, electrochemical, melting points, and maximum solubility for the oligomer series **1-5** in comparison to $PC_{61}BM$.

Oligomer	λ_{abs} sol [nm][a]	ε [M^{-1} cm^{-1}]	ΔE_{opt} sol [eV]	λ_{abs} film [nm][b]	ΔE_{opt} film [eV]	E^0_{ox1} [V][c]	E^0_{ox2} [V][c]	E^0_{red1} [V][c]	HOMO [eV][d]	LUMO [eV][d]	ΔE_{CV} [eV]	T_m [°C][e]	Solubility [mg/mL][f]
1	488	74 900	2.25	530	2.04	0.75	0.89	-1.62	-5.8	-3.7	2.1	156	>120
2	500	67 300	2.10	576, 620	1.82	0.64	0.82	-1.43	-5.7	-3.8	1.9	244	1
3	519	62 100	2.01	604, 649	1.76	0.49	0.68	-1.45	-5.5	-3.7	1.8	215	1
4	552	60 900	1.84	631, 677	1.66	0.36	0.61	-1.47	-5.4	-3.8	1.6	270	2
5	560	58 400	1.81	653, 696	1.60	0.27	0.63	-1.47	-5.3	-3.7	1.6	180	>120
$PC_{61}BM$	329	40 100	3.08	-	-	-	-	-	-6.1	-4.0	2.1	-	28

[a]Absorption spectra were measured in dichloromethane. [b]Thin films were spin-coated from chloroform solutions (4 mg/mL) on glass substrate at 3000 rpm. [c]Cyclic voltammetry in dichloromethane/$TBAPF_6$ (0.1 M), scan rate = 100 mV/s, referenced against Fc/Fc$^+$. The redox potentials ($E°_{ox}$ and $E°_{red}$) were calculated by the mean of the cathodic and anodic peak potentials of a quasi-reversible waves: $E° = (E_{pa}+E_{pc})/2$. For the irreversible waves, the redox potentials $E°$ were determined at $I_0 = 0.852I_p$.[56] [d]HOMO/LUMO energy values were calculated by setting Fc/Fc$^+_{vac}$ at -5.1 eV vs vacuum. [e]Melting temperature (T_m) was determined using differential scanning calorimetry. [f]Solubility was measured in chloroform.

The redox properties of oligomers **1-5** were determined by cyclic voltammetry. In Figure 3 and Table 1, the results of the electrochemical measurements are displayed. Cyclic voltammograms of oligomers **1-5** generally showed two reversible oxidation waves, which are assigned to the formation of stable radical cations and dications delocalized over the conjugated backbone. In contrast, only one irreversible reduction wave was observed upon a negative potential scan which is assigned to the simultaneous radical anion formation located on the terminal DCV groups. The E_p values for the reduction waves are given in Table S1 (supporting information).

The energy levels of the frontier orbitals were determined from the onset of the first oxidation and reduction potential and are important parameters for the function of an organic solar cell. The lowest unoccupied molecular orbital (LUMO) of all five oligomers did not vary a lot in the series and their energy was found between -3.7 and -3.8 eV. A value of -3.7 eV should be ideal for maximizing the open-circuit potential (V_{OC}) of the solar cell devices, while allowing sufficient offset to the LUMO of $PC_{61}BM$ (-4.0 eV) to ensure efficient electron transfer. With increasing donor strength of the central building block of oligomers **1** through **5**, the HOMO energy level gradually increased from -5.8 eV for carbazole derivative **1** to -5.3 eV for dithieno[3,2-*b*:2',3'-*d*]pyrrole-based oligomer **5**. Both trends are reflected in an energy level diagram, which compares the HOMO and LUMO energies of the new oligomers with the energy level of $PC_{61}BM$ (Figure 4). In this series of molecules **1-5** a correlation of the molecular structures with respect to the effect of central donor moieties on optical and electrochemical properties could be realized.

Another relevant parameter for the fabrication of solution-processed solar cells is favorable film formation, for which good solubilities of both, the donor and the acceptor, in organic solvents are a prerequisite. The maximum solubility of all oligomers **1-5** was determined in chloroform solution and the values are summarized in Table 1. Oligomers **1** and

5 have the same number and length of alkyl chains along their backbone yielding high solubilities of >120 mg/mL. In contrast, oligomers **2** and **3** bear no alkyl chains on their central building block which results in a decrease in solubility by two orders of magnitude for both derivatives (1 mg/mL). Octyl-substituted dithieno[3,2-*b*:2',3'-*d*]silole-containing oligomer **4** also showed a lower solubility of only 2 mg/mL. Thermal behavior of **1**–**5** were investigated using differential scanning calorimetry (DSC) (Figure S1, Supporting information). It should be noted that, despite having longer octyl chains, oligomer **4** displayed the highest melting temperature (T_m) (Table 1) among all oligomers indicating extensive crystallinity in the solid state. The same phenomenon has been observed for conjugated polymers comprising silole units which, compared to their carbon based analogues, showed increased crystallinity and dramatically decreased solubility.[57,58]
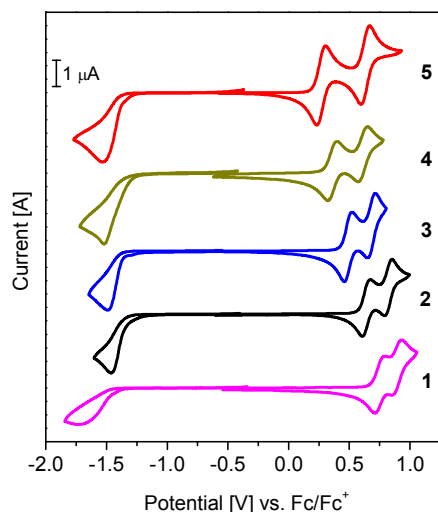
Figure 3. Cyclic voltammograms of oligomers **1-5** in dichloromethane, TBAPF$_6$ (0.1 M) measured versus the ferrocene/ferricenium (Fc/Fc$^+$) redox couple.
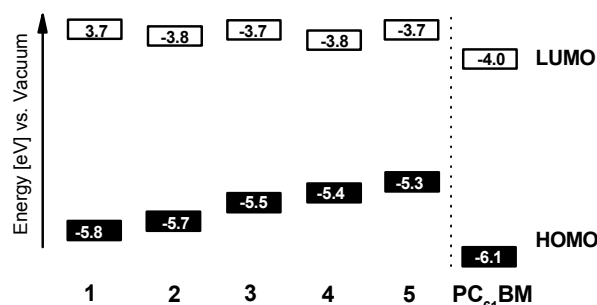
Figure 4. Energy level diagram of the donor materials **1-5** in comparison to the $PC_{61}BM$ acceptor.

In order to obtain some deeper insight into the packing behavior of oligomers **1-5** in the solid state, grazing incident X-ray diffraction (GIXRD) experiments were firstly performed on neat films. The resulting diffraction patterns are plotted in Figure 5. All oligomers displayed a relatively intense (100) reflection peak at low angle ($2\theta = 5.16°$ for **1**, $6.43°$ for **2**, $6.60°$ for **3**, $4.92°$ for **4**, and $4.90°$ for **5**) indicating the presence of some crystalline domains. This low angle reflection is assigned to the d_{100} spacing between two adjacent oligothiophenes backbone, and its value is directly related to the presence (or lack thereof) of alkyl chains on the central building block. Oligomers **1**, **4**, and **5** (with alkyl chains) showed a d_{100} spacing of 17.1 Å, 17.9 Å and 18.0 Å, whereas oligomers **2** and **3** (without alkyl chains) pack more densely giving d_{100} spacing of 13.7 Å and 13.4 Å, respectively. Such XRD experiments on the neat films give qualitative information regarding the packing behavior of the molecules and facilitate peak assignment in the diffraction pattern obtained for the blend films.
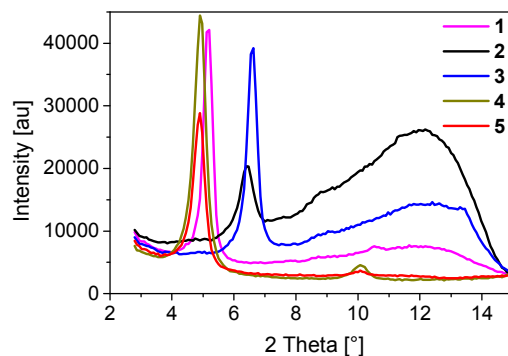
Figure 5. GIXRD plot of neat films consisting of oligomers **1-5**.

Solution-processed bulk-heterojunction solar cells were fabricated using oligomers **1-5** as electron donors in combination with $PC_{61}BM$ as electron acceptor. D:A ratio, solvent, solvent for the SVA as well as annealing time were all investigated with respect to their effect on photovoltaic performance. The characteristics of the best performing solar cells for oligomers **1-5** after SVA are tabulated in Table 2 and compared to their performance without SVA treatment. As previously mentioned, oligomer **1** displayed the largest HOMO-LUMO energy gap (2.0 eV) and thus the deepest HOMO energy level whereas oligomer **5** had the smallest energy gap (1.6 eV) due to the highest HOMO energy level. In the working solar cell device, this trend correlates to the value of the open-circuit voltage (V_{OC}). For oligomers **1-5** the V_{OC} of the solar cells gradually decreased from 1.15 V for **1** to 0.84 V for **5**.

All active blend layers containing **1-5** reacted positively to the SVA treatment as shown in Table 2. The SVA process mostly enhances J_{SC} and FF resulting in an improved PCE depicted in Figure 6 for all oligomers. For the carbazole-containing oligomer **1**, the efficiency increased from 0.03 to 1.4% when the active layer was exposed to THF vapor, mostly due to an enhancement in the J_{SC} and FF values. In the case of oligomer **2**, comprising a benzo[2,1-*b*:3,4-*b'*]dithiophene central unit, the PCE increased from 0.4 to 2.6% using $CHCl_3$ for SVA. When 2,2'-bithiophene was used as the central block in **3**, then a PCE of 1.4% was measured before SVA which dramatically increased to 5.8% after SVA. For both, oligomers **2** and **3**, the J_{SC} values were increased by a factor of 2-3 and the FF was almost doubled after SVA. The dithieno[3,2-*b*:2',3'-*d*]silole-based oligomer **4** displayed the smallest increase in PCE, from 2.3 to 3.8%, upon exposure to solvent vapor. Finally, the dithieno[3,2-*b*:2',3'-*d*]pyrrole analogue **5** showed a PCE of 1.3% before SVA and 5.9% after exposure to $CHCl_3$ vapor. This is very similar to the value of 6.1% reported earlier for oligomer **5**, supporting good batch-to-batch reproducibility of the results even in other laboratory.[21] In Figure 6, the impact of SVA on the

PCE is shown graphically. It is noteworthy to mention that in the case of oligomer **1**, regardless of large changes in the processing conditions such as D:A ratio, solvent, or active layer thickness, the PCEs remained around 1%, as a result of low J_{SC} values despite very good FFs. We believe that this can be attributed to the HOMO energy level of **1** being very close to that of the HOMO energy of the electron acceptor $PC_{61}BM$, thus resulting in competition between electron and energy transfer between the donor and acceptor units.[59] This conclusion is supported by both, the lower J_{SC} value of 1.4 mA cm^{-2} and the saturation value of 1.10. It is also possible that the performance of solar cells containing oligomer **2** also suffer for the same reason, however, to a lesser extent due to its slightly higher HOMO level. Oligomers **3-5** with increasingly higher HOMO energy levels of -5.5 to -5.3 eV seem to be sufficient to allow fabrication of efficient solar cell devices.

Table 2. Photovoltaic parameters of solar cells fabricated before and after solvent vapor annealing (SVA). Device structure: ITO| PEDOT:PSS| **Oligomer**:$PC_{61}BM$| LiF| Al.

Donor	D:A ratio	SVA [s]	J_{SC} [mAcm^{-2}]	V_{OC} [V]	FF	PCE [%]	Saturation^a
1	1:1	0	0.1	1.05	0.26	0.03	2.22
1	1:1	THF, 60	2.1	1.15	0.57	1.4	1.10
2	1:2	0	1.3	1.02	0.29	0.4	1.76
2	1:2	$CHCl_3$, 45	4.4	1.11	0.54	2.6	1.13
3	1:2	0	4.2	1.03	0.32	1.4	1.49
3	1:2	$CHCl_3$, 45	8.5	1.01	0.68	5.8	1.06
4	1:2	0	4.8	0.89	0.55	2.3	1.21
4	1:2	$CHCl_3$, 60	6.4	0.88	0.69	3.8	1.07
5	1:2	0	4.2	0.84	0.35	1.3	1.55
5	1:2	$CHCl_3$, 30	9.8	0.84	0.72	5.9	1.04

^{a}Saturation defined as J_{-1V}/J_{SC}.
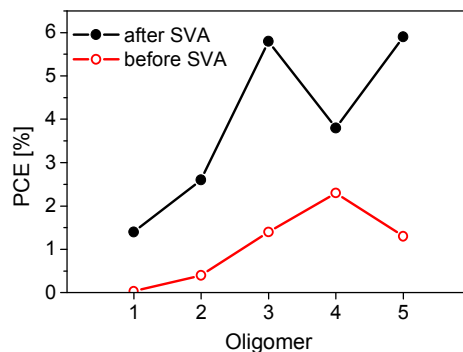
Figure 6. Plot of the PCE variations for each compound before and after solvent vapor annealing.

Considering the above facts, for the remainder of this contribution, we will only discuss the solar cell results and the interpretation thereof for the more efficient oligomers **3**-**5**. Figure 7 shows the *J-V* curves and external quantum efficiency (EQE) plot of donors **3**-**5**:PC$_{61}$BM-based devices before and after SVA. The significant improvement of J_{SC}, FF, and PCE as a result of exposure to solvent vapor is demonstrated. If all three oligomers had the same D:A phase-separated morphology after the SVA process, then one would expect there to be a trade-off between the optical gap of the donor and J_{SC} values in the photovoltaic devices. This is in fact observed for oligomers **3** and **5**, however, in the case of oligomer **4** it is not seen. The J_{SC} of oligomer **4** was measured to be 6.4 mA cm^{-2}, which is lower compared to **3** (8.5 mA cm^{-2}) and **5** (9.8 mA cm^{-2}), most likely due to non-optimal D:A phase separation. For **3** and **5**, the product of the J_{SC} and V_{OC} values are comparable resulting in similar overall PCEs of 5.8 and 5.9%, respectively. The trend in the obtained photocurrent from the *J-V* measurement for **3**-**5** was also observed in the EQE spectra. The EQE spectra of the oligomers are shown in Figure 7b. The maximum EQE of oligomer **4** is lower than the EQE of oligomers **3** and **5**. For all oligomers, the conversion of photons to electrons is significantly improved after SVA. For oligomer **3**, the maximum EQE before treatment with solvent vapor was measured to 37%@440 nm, however, both, an improvement in EQE maximum to 57% as well as a large red-shift of the spectral maximum to 580 nm was achieved. For oligomer **4**-

based devices, the EQE profile showed nearly a similar feature with the maximum EQE increased from 30 to 40% @630 nm after SVA. In the case of oligomer **5**, exposure to chloroform vapor led to both, a spectral broadening and an enhancement of the EQE from 40 to 52% @640 nm.
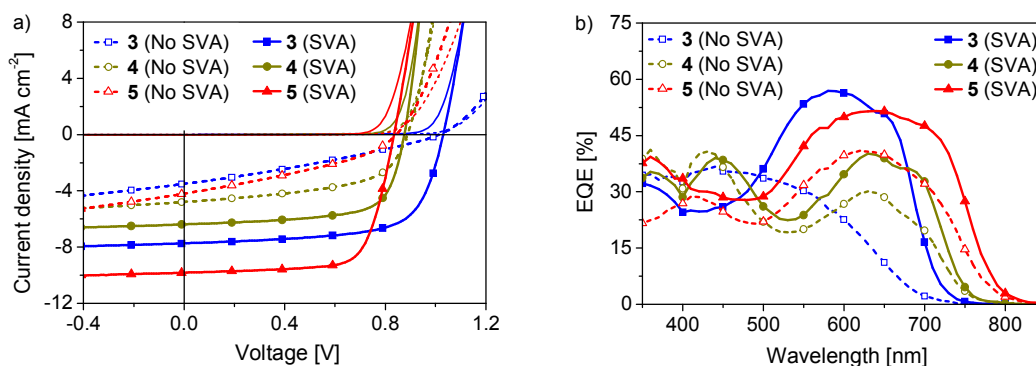
Figure 7. (a) *J-V* curve of solution-processed solar cells containing oligomers **3-5** as donor and PC$_{61}$BM as acceptor. (b) EQE spectra of the corresponding BHJ devices before and after SVA. Device structure: ITO| PEDOT: PSS| **Oligomer**:PC$_{61}$BM(1:2)| LiF| Al.

Further study of the photoactive layers was carried out using UV-vis absorption and GIXRD techniques (Figure 8). To various extents, the absorption spectra of the blend films were influenced by exposure to organic solvent vapor. The absorption profile of oligomer **3**:PC$_{61}$BM blends displayed an increase in intensity and a red-shift of 21 nm with the appearance of a vibronic shoulder at 650 nm (Figure 8a). In the case of oligomer **4**, SVA had little influence on the active layer absorption with slight increase in intensity. Finally, the **5**:PC$_{61}$BM-containing films showed enhanced absorption concomitant with a red-shift of 19 nm and the formation of a shoulder at 700 nm upon SVA. In general, both, the increase in intensity and the red-shift of the absorption, is attributed to reorientation and reorganization of the donor molecules in the blend leading to an enhancement in the absorption cross-section of the films as well as their planarization.
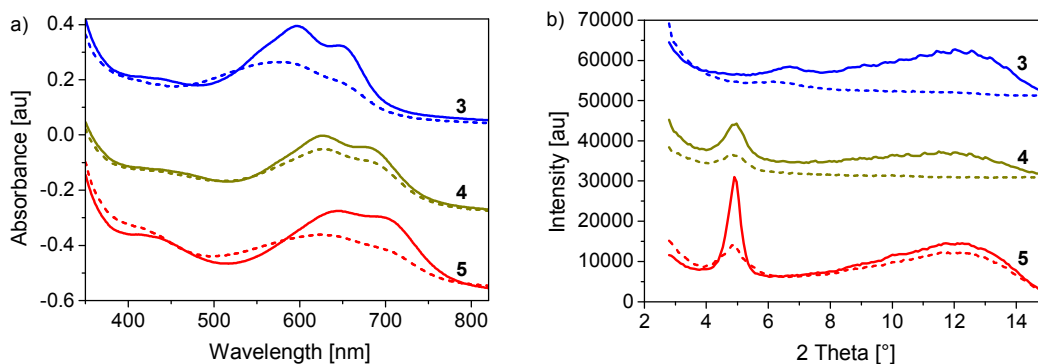
Figure 8. (a) Normalized absorption spectra of **3-5**:$PC_{61}BM$ blend films prepared with before and after SVA. (b) GIXRD plot of the BHJ made using the same conditions. Dashed lines: before SVA, solid lines: after SVA. All films were spin-coated on PEDOT:PSS to reproduce the active layer as used for solar cells.

The diffraction patterns of the GIXRD experiments before and after the SVA process also provided some insight into the organization and ordering in the D:A blend films containing oligomers **3** through **5** (Figure 8b). The presence of the peak for all blend films at low angle reflection ($2\theta = 6.67°$ for **3** and $4.90°$ for **4** and **5**) originates from the donor molecules. A d_{100} spacing of 13.2 Å was calculated for oligomer **3**, whereas **4** and **5** showed a larger spacing of 18 Å. For all oligomers, especially **4** and **5**, the intensity of the 100-peak is notably increased after exposure to chloroform vapor. The analogous UV-vis and GIXRD experiments for blends containing oligomers **1** and **2** showed the same trends as seen in Figure 8 and can be found in the Supporting Information (Figure S2).

The surface morphology of the D:A blends was investigated using atomic force micros-copy (AFM). Each sample was prepared by spin-coating the donor:$PC_{61}BM$ blend onto ITO/PEDOT:PSS, accurately reproducing the photoactive layer of the corresponding devices. Figures 9a-c' depict the topography (a-c) and phase images (a'-c') of blends containing **3-5**:$PC_{61}BM$ before SVA treatment, whereas Figures 9d-f' display the analogous images for the same blends after SVA. The topography roughness (R_q) of the blend films was extracted from the height images. The blend films of **3-5**:$PC_{61}BM$ before SVA have a R_q of 0.4 ± 0.1 nm, 1.8

± 0.1, and 0.4 ± 0.1 nm for **3** through **5**, respectively. After the solvent vapor annealing process the topography roughness increased to 1.6 ± 0.1 nm, 1.9 ± 0.2, and 1.1 ± 0.1 nm in the same sequence.

Compared to the topography images, the phase-shift signal of the cantilever oscillation typically yields better contrast and is more sensitive to variations in the compositions. Therefore, we also show the phase images in Figure 9, where regions of bright and dark contrast are distinguishable, in order to evaluate the active layer film morphology. Worm-like structures showing domain sizes between 10-30 nm are visible for **3**:$PC_{61}BM$-based blends before SVA (Figure 9a'). This blend, when exposed to $CHCl_3$ vapor (Figure 9d'), displayed D:A domains of increased size (20-80 nm). Photoactive layers containing **4**:$PC_{61}BM$ (Figure 9b', 9e') appeared very similar and remained largely unaffected by the SVA process. In the case of the D:A blend consisting of oligomer **5**, before SVA, phase separation is not evident (Figure 9c'). After exposure to chloroform vapor (Figure 9f'), the structure developed clearer phase separation, and domains of 20-50 nm in size are visible. We conclude that for this series of oligomers, the SVA process leads to an increase in topography roughness and to the formation of a more distinct bi-continuous network of donor and acceptor-rich domains.
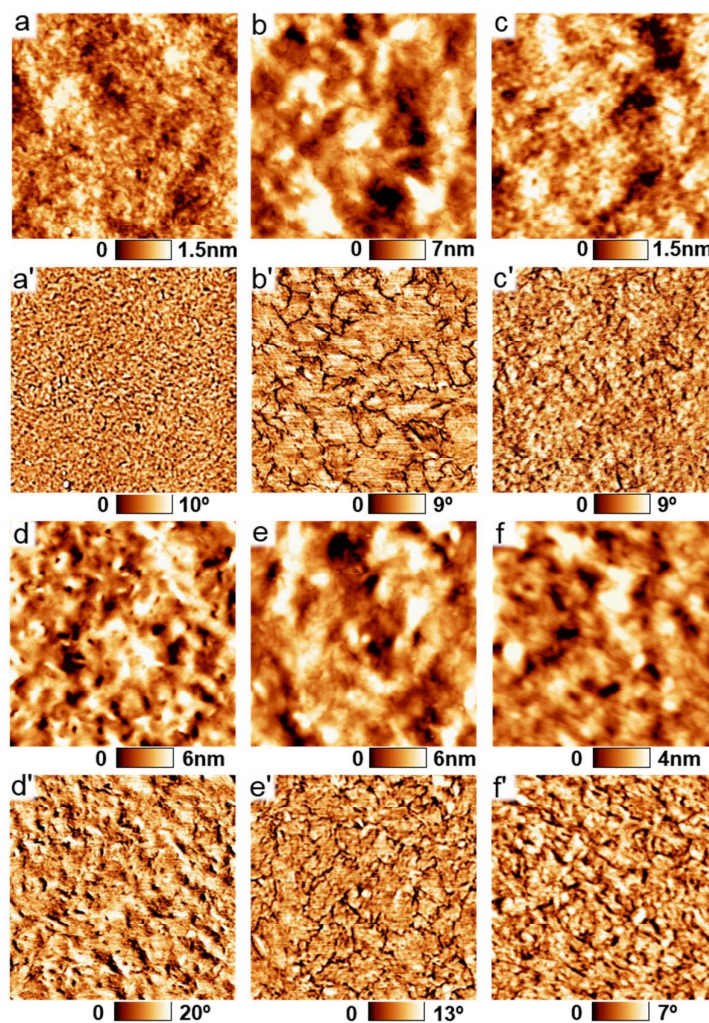
Figure 9. AFM topography and corresponding phase images of donor:PC$_{61}$BM blends spin-coated on ITO| PEDOT:PSS: a) a') **3** from TCE, b) b') **4** from CHCl$_3$, c) c') **5** from CHCl$_3$ before SVA and d) d') **3** from TCE, e) e') **4** from CHCl$_3$, f) f') **5** from CHCl$_3$ after SVA. Image size: 1 μm × 1 μm.

All active layers containing oligomers **1-5** reacted positively to the SVA treatment as shown in Table 2 and Figures 6 and 7. This finding is certainly related to their chemical structure, but also to the deposition conditions used to prepare the photoactive layer. In general, the exposure to organic vapors results in more distinct D:A phase separation and increased domain size.[15, 45, 49, 63] This process is likely comparable to thermal annealing, where it has also been shown that the domain size increase upon annealing time.[1, 44, 64] For successful SVA, i.e. maximizing the PCE, one would ideally produce a very well mixed D:A film after the spin-coating process with very fine phase separation. The measured *J-V* characteristics

would be poor, i.e, low J_{SC}, low FF, and poor saturation value due to a large amount of charge recombination. Upon SVA, a well-defined D:A phase separation would be formed resulting in an enhancement of the aforementioned photovoltaic parameters and thus of the PCE. Both the exposure time to the solvent and the solvent vapor pressure play a vital role in tuning the active layer D:A morphology. If one considers the photovoltaic parameters of the cells based on oligomers **1-5** before SVA shown in Table 2, the data indicates that the desired well mixed blend is indeed produced. Upon SVA of the corresponding blends, the J_{SC} and FF values are increased substantially with lowering of the saturation due to efficient charge separation and extraction. The overall enhancement of the PCE as a result of SVA treatment for each oligomer in the series is clearly visible in Figure 6.

Conclusions

In summary, we have presented synthesis and characterization of a new series of A-D-A oligomers **1-5** for application in solution-processable bulk-heterojunction solar cells. The influence of the central conjugated core unit on the optoelectronic and photovoltaic properties of the oligomers was evaluated. A systematic red-shift of the absorption spectra in solution and thin films, increase of the HOMO energy level and reduction of the HOMO-LUMO energy gap was achieved by increasing the donor strength of the central block of the oligomers on going from **1** through **5**. The carbazole derivative **1** had the lowest HOMO level of -5.8 eV which was too deep for efficient electron transfer to $PC_{61}BM$, thus resulting in a lower PCE of 1.4%. The increase of the HOMO level was directly correlated with the decrease of the V_{OC} value while going from oligomer **1** to **5**. All donor materials responded positively to solvent vapor annealing which was evidenced by significant improvement of J_{SC} and FF. For oligomers **3** and **5**, a trade-off between J_{SC}, and V_{OC} was seen due to their differing energy gaps resulting in similar PCEs of 5.8 and 5.9%, respectively. The device

performance was further correlated with the nanoscale morphology of the photoactive layers which was investigated by thin film absorption, XRD, and AFM measurements. The results suggested that the D:A blend films exhibit increased crystallinity and efficient nanoscale phase separation upon SVA. Our results indicate that the optoelectronic and the photovoltaic properties of organic semiconductors can be fine-tuned by judicious design of the molecular backbone.

Experimental Section

Materials and Methods: Tetrabutylammonium hydroxide, tris(dibenzylideneacetone)di-palladium(0), and tri(*o*-tolyl)phosphine were purchased from Alfa Aesar. Malononitrile was purchased from Merck. The building blocks 9-(2-hexyldecyl)-2,7-bis(4,4,5,5-tetramethyl-1,3,2-dioxaborolan-2-yl)carbazole **5**,[60] 5,5'-bis(trimethylstannyl)-2,2'-bithiophene **6**,[61] 2,7-bis(trimethylstannyl)benzo[2,1-*b*:3,4-*b*']dithiophene **7**,[62] and 4,4-dioctyl-2,6-bis(trimethylstannyl)-dithieno[3,2-*b*:2',3'-*d*]silole **8**,[63] as well as bromo derivatives 5'-Bromo-3,4'-dihexyl-2,2'-bithiophene-5-carbaldehyde **9** and 2-((5'-bromo-3,4'-dihexyl-[2,2'-bithien]-5-yl)methylene)-malononitrile **10**[64] were prepared according to literature procedures. *N*,*N*-Dimethylformamide (Merck) was dried via MB SPS-800 solvent purifying system (MBraun). All synthetic steps were carried out under argon atmosphere. Preparative column chromatography was performed on glass columns packed with silica gel (Merck Silica 60, particle size 40-43 μm). High performance liquid chromatography (HPLC) was performed on a Hitachi instrument equipped with a UV-vis detector L-7420, columns (Nucleosil 100-5 NO₂ with a pore size of 100 Å) from Machery-Nagel using a dichloromethane/n-hexane mixture (40:60) as eluent. NMR spectra were recorded on a *Bruker* Avance 400 spectrometer (^{1}H NMR: 400 MHz, ^{13}C NMR: 100 MHz) or a *Bruker* AMX 500 (^{13}C NMR: 125 MHz) at 25 °C or 100 °C, respectively. Chemical shift values (δ) are expressed in parts per million using residual solvent protons (^{1}H

NMR, δ_H = 7.26 for CDCl$_3$ and δ_H = 5.93 for 1,1,2,2-tetrachloroethane (TCE)-d$_2$; ^{13}C NMR, δ_C = 77.0 for CDCl$_3$ and δ_C = 74.20 for TCE-d$_2$) as internal standard. The splitting patterns are designated as follows: s (singlet), d (doublet), and m (multiplet). EI mass spectra (GC-MS) were recorded on a *Varian* Saturn *2000* and MALDI-TOF mass spectra on a *Bruker* Daltonic Reflex III using dithranol or DCTB (trans-2-[3-(4-tert-butylphenyl)-2-methyl-2-propenylidene]malononitrile) as matrices. Melting points were determined using a Büchi B-545 apparatus and were not corrected. Elemental analyses were performed on an Elementar Vario EL.

Optical solution measurements were carried out in 1 cm cuvettes with Merck Uvasol grade solvents; absorption spectra were recorded on a Perkin Elmer Lambda 19 spectrometer. Maximum solubility values were measured using UV-vis absorption spectroscopy. After determination of the molar extinction coefficient, saturated solutions were made, stirred for 60 min at 60 °C and then allowed to cool to room temperature. The saturated solutions were then filtered and diluted for absorption spectroscopy and consequently the corresponding concentrations could be determined. The absorption spectra in thin films were prepared by spin-coating from chloroform solution (4 mg/mL) on a glass substrate at 3000 rpm. Cyclic voltammetry experiments were performed with a computer-controlled Metrohm Autolab PGSTAT30 potentiostat in a three-electrode single-compartment cell with a platinum working electrode, a platinum wire counter electrode, and an Ag/AgCl reference electrode. All potentials were internally referenced to the ferrocene/ferricenium couple (-5.1 eV vs. vacuum). The characterization of the surface topography was performed using an atomic force microscope (MultiMode V SPM, Bruker). The microscope was operated in air (at about 25 °C) in the tapping mode using silicon commercial tips with resonance frequency of 200-400 kHz and a spring constant of $\approx$ 50 N m^{-1}. The images were analyzed with the help of the WSxM software.[65]

Device Fabrication: Photovoltaic devices were made by spin-coating PEDOT:PSS (Clevios P, VP Al4083) onto pre-cleaned, patterned indium tin oxide (ITO) substrates (13-15 Ω per square) (Naranjo). The photoactive layer (80-90 nm) was deposited by spin-coating from of a mixed solution of donor and $PC_{61}BM$ acceptor (weight-ratio 1:2). $PC_{61}BM$ was purchased from Solenne BV, Netherlands. Depending on the oligomer, different solvents and deposition temperatures were used for active layer deposition (**1**: CB 80 °C, **2** and **3**: TCE 120 °C, **4** and **5**:CHCl$_3$ at 60 °C and 50 °C). The solvent vapour annealing (SVA) was carried out by dropping 100 μL THF or CHCl$_3$ around the as-cast BHJ layer and covering with a petri dish in a way that the film is exposed to CHCl$_3$ atmosphere for 30–60 s (Table 2). The counter electrode of LiF (1 nm) and aluminum (100 nm) was deposited by vacuum evaporation at 2 x 10^{-6} Torr. The active areas of the cells were either 0.09 or 0.16 cm^2. No solar cell performance dependence on active area was observed. Film thicknesses were measured using a Dektak profilometer. *J-V* characteristics were measured under AM 1.5G conditions at 100 mWcm^{-2} with a AAA solar simulator from Oriel Instruments using a Keithley 2400 source meter. Spectral response (EQE) was measured under monochromatic light from a 300 W Xenon lamp in combination with a monochromator (Oriel, Cornerstone 260) modulated with a mechanical chopper. The response was recorded as the voltage over a 220 Ω resistance using a lock-in amplifier (Merlin 70104). A calibrated Si cell was used as reference.

Synthesis: *2,2'-([5',5'''-(9-(2-hexyldecyl)carbazole-2,7-diyl)bis(3,4'-dihexyl-2,2'-bithiene-5',5-diyl)]bis(methanylylidene))dimalononitrile* **1**: 9-(2-hexyldecyl)-2,7-bis(4,4,5,5-tetra-methyl-1,3,2-dioxaborolan-2-yl)carbazole **5** (0.082 g, 0.127 mmol) was combined with 5'-bromo-3,4'-dihexyl-2,2'-bithiophene-5-carbaldehyde **9** (0.135 g, 0.305 mmol) in degassed toluene (4 mL) and degassed 20% aqueous tetrabutylammonium hydroxide (1.3 mL), to which tris(dibenzylideneacetone)dipalladium(0) (1.2 mg, 1.3 μmol) and tri(*o*-tolyl)phosphine (1.5 mg, 4.9 μmol) were added. The reaction was heated to 90 °C for 48 hours, after which the

reaction was allowed to cool to room temperature, reduced in volume, ran over a celite plug and then through a short SiO_2 column using dichloromethane as eluent. The resulting solution was again reduced in volume and dried. A 1:1-volume mixture of dichloroethane and ethanol (4 mL) was added to the reaction flask, followed by malononitrile (0.025 g, 0.38 mmol) and ammonium acetate (4 mg, 0.054 mmol). The reaction mixture was heated to 80 °C for 36 hours. Upon cooling to room temperature, all solvents were removed and the crude product was dissolved in dichloromethane. The organic phase was washed with water (2x) and then with a brine solution. The organic phase was dried over $MgSO_4$, filtered and the solvents were removed *in vacuo*. Gradient column chromatography (silica gel, petroleum ether:dichloro-methane 1:1 → 1:2) was performed, followed by HPLC for the final purification. Carbazole-oligomer **1** (0.061 g, 0.05 mmol, 40%) was obtained as a dark red solid by precipitation in methanol. Mp: 156 °C. ^{1}H NMR (400 MHz, $CDCl_3$) δ = 8.15 (d, *J* = 8 Hz, 2H), 7.71 (s, 2H), 7.55 (s, 2H), 7.47 (s, 2H), 7.36 (d, *J* = 8 Hz, 2H), 7.32 (s, 2H), 4.21 (d, *J* = 7.4 Hz, 2H), 2.88 (t, *J* = 7.8 Hz, 4H), 2.77 (t, *J* = 7.8 Hz, 4H), 2.17 (s, 1H), 1.70 (m, 8H), 1.5-1.1 (m, 48H), 0.86 (m, 18H). ^{13}C NMR (100 MHz, $CDCl_3$) δ = 150.36, 145.00, 143.26, 142.30, 141.88, 140.78, 140.28, 132.48, 132.20, 131.57, 131.47, 122.64, 121.02, 120.98, 114.86, 113.92, 110.03, 48.37, 38.45, 31.40, 30.00, 29.63, 29.26, 27.01, 22.98, 22.94, 14.42. HR-MS (MALDI-TOF): *m/z* [M$^+$] = 1207.6616 (calc. for $C_{76}H_{97}N_5S_4$: 1207.6627, δm/m = 0.91 ppm).

2,2'-([5',5'''-(Benzo[2,1-b:3,4-b']dithiene-2,7-diyl)bis(3,4'-dihexyl-2,2'-bithiene-5',5-diyl)]bis(methanylylidene))dimalononitrile **2**: A mixture of 2,7-bis(trimethylstannyl)ben-zo[2,1-*b*:3,4-*b*']dithiophene **6** (0.200 g, 0.39 mmol), 2-([5'-bromo-3,4'-dihexyl-2,2'-bithien-5-yl]methylene)malononitrile **10** (0.475 g, 0.97 mmol), and Pd(PPh$_3$)$_4$ (30 mg, 26 μmol) in 13 mL DMF were heated to 80 °C for 14 h. After cooling, the solvent was removed and the crude product was purified by column chromatography (flash silica, *n*-hexane/DCM 1:1 - 1:4). Further purification was done using high performance liquid chromatography. Product **2**

(0.369 g, 0.37 mmol, 94%) was obtained as a dark purple solid by precipitation in methanol.

Mp: 244 °C. ^{1}H NMR (400 MHz, CDCl$_3$): δ = 7.77 (s, 2H), 7.71 (s, 2H), 7.54 (s, 2H), 7.51 (s, 2H), 7.27 (s, 2H), 2.92-2.84 (m, 8H, CH$_2$), 1.74-1.69 (m, 8H, -CH$_2$-), 1.49-1.42 (m, 8H, -CH$_2$-), 1.37-1.33 (m, 16H, - CH$_2$-), 0.93-0.88 (m, 12H, CH$_3$). ^{13}C NMR (125 MHz, CDCl$_3$, 330K): δ = 149.84, 143.59, 142.12, 141.41, 137.99, 134.18, 134.14, 133.53, 133.19, 132.65, 131.64, 124.18, 121.23, 114.39, 113.53, 31.79, 31.76, 30.71, 30.27, 29.66, 29.51, 29.37, 29.29, 22.73, 14.13. MS (MALDI-TOF): m/z [M+] = 1006.2 (calc. for C$_{58}$H$_{62}$N$_4$S$_6$: 1006.33). Elemental analysis for C$_{58}$H$_{62}$N$_4$S$_6$: C, 69.14; H, 6.20; N, 5.56; S, 19.10 found: C, 69.35; H, 6.04; N, 5.49; S, 19.22.

2,2'-([3,4',3'''',3'''''-Tetrahexyl-(2,2':5',2'':5'',2''':5''',2'''':5'''',2'''''-sexithiene-5,5'''''-diyl)]- bis(methanylylidene))dimalononitrile **3**: A mixture of 5,5'-bis(trimethylstannyl)-2,2'-bithiophene **7** (0.075 g, 0.152 mmol), 2-([5'-bromo-3,4'-dihexyl-2,2'-bithien-5-yl]methylene)malononitrile **10** (0.179 g, 0.366 mmol), and Pd(PPh$_3$)$_4$ (8.8 mg, 7.1 μmol) in 5 mL DMF were heated to 80 °C for 24 h. After cooling, the solvent was removed and the crude product digested with ethyl acetate:petroleum ether 1:2, followed by purification by column chromatography (flash silica, dichloromethane). Further purification was performed by high performance liquid chromatography and the desired product (0.117 g, 0.119 mmol, 78%) was obtained as a metallic green solid after precipitation in methanol. Mp: 215 °C. ^{1}H NMR (500 MHz, TCE-d$_2$, 373K): δ = 7.64 (s, 2H), 7.54 (s, 2H), 7.19 (s, 2H), 7.18 (d, J = 3.8 Hz, 2H,), 7.12 (d, J = 3.8 Hz, 2H), 2.82 (m, 8H, CH$_2$), 1.71 (m, 8H, -CH$_2$-), 1.48-1.23 (m, 24H, -CH$_2$-), 0.90 (m, 12H, CH$_3$). ^{13}C NMR (125 MHz, TCE-d$_2$, 373K): δ = 149.78, 143.86, 141.54, 141.37, 137.84, 134.85, 134.23, 132.60, 132.35, 131.62, 127.66, 124.78, 120.63, 114.53, 113.62, 99.94, 31.75, 31.70, 30.51, 30.17, 29.65, 29.50, 29.29, 29.20, 22.69, 14.10. HR-MS (MALDI-TOF): m/z [M+] = 982.3295 (calc. for C$_{56}$H$_{62}$N$_4$S$_6$: 982.3299, δm/m = 0.41 ppm).

2,2'-([5',5'''-(4,4-Dioctyldithieno[3,2-b:2',3'-d]silole-2,6-diyl)bis(3,4'-dihexyl-2,2'-bithie-ne-5',5-diyl)]bis(methanylylidene))dimalononitrile **4**: A mixture of 4,4-dioctyl-2,6-bis(trime-thylstannyl)-dithieno[3,2-*b*:2',3'-*d*]silole **8** (0.12 g, 0.16 mmol), 2-([5'-bromo-3,4'-dihexyl-2,2'-bithien-5-yl]methylene)malononitrile **10** (0.197 g, 0.4 mmol), and Pd(PPh$_3$)$_4$ (7.4 mg, 6.4 μmol) in 5 mL DMF were carefully degassed and heated to 80 °C for 20 h. After cooling, the solvent was removed and the crude product was purified by column chromatography on silica gel (gradiant DCM/n-hexane 2:1→3:1) to yield pure oligomer **4** as a dark green solid (0.165 g, 0.13 mmol, 83%). Mp: 270 °C. ^{1}H NMR (500 MHz, TCE-d$_2$, 373K): δ = 7.69 (s, 2H), 7.52 (s, 2H), 7.23 (s, 2H), 7.17 (s, 2H), 2.83 (m, 8H, -C*H*$_2$-), 1.69 (m, 8H, -C*H*$_2$-), 1.15-1.50 (m, 52H, -C*H*$_2$-), 0.78-1.0 (m, 22H, C*H*$_3$). HRMS (MALDI-TOF): m/z [M+] = 1235.0430 (calc. for C$_{72}$H$_{94}$N$_4$S$_6$Si: 1234.5632, δm/m = 0.39 ppm). Elemental analysis for C$_{72}$H$_{94}$N$_4$S$_6$Si: C, 69.96; H, 7.67; N, 4.53; S, 15.57 found: C, 69.93; H, 7.57; N, 4.43; S, 15.80.

References

1. B. Walker, A. B. Tamayo, X.-D. Dang, P. Zalar, J. H. Seo, A. Garcia, M. Tantiwiwat and T.-Q. Nguyen, *Adv. Funct. Mater.*, 2009, **19**, 3063-3069.
2. A. Mishra and P. Bäuerle, *Angew. Chem. Int. Ed.*, 2012, **51**, 2020–2067.
3. Y. Chen, X. Wan and G. Long, *Acc. Chem. Res.*, 2013, **46**, 2645-2655.
4. J. E. Coughlin, Z. B. Henson, G. C. Welch and G. C. Bazan, *Acc. Chem. Res.*, 2014, **47**, 257–270.
5. C. Brabec, V. Dyakonov and U. Scherf, eds., *Organic Photovoltaics – Materials, Device Physics and Manufacturing Technologies*, 2nd Ed. edn., Wiley-VCH verlag, Weinheim, 2014.

6. X. Xiao, G. Wei, S. Wang, J. D. Zimmerman, C. K. Renshaw, M. E. Thompson and S. R. Forrest, *Adv. Mater.*, 2012, **24**, 1956–1960.
7. H. Bürckstümmer, E. V. Tulyakova, M. Deppisch, M. R. Lenze, N. M. Kronenberg, M. Gsänger, M. Stolte, K. Meerholz and F. Würthner, *Angew. Chem. Int. Ed.*, 2011, **50**, 11628–11632.
8. A. Zitzler-Kunkel, M. R. Lenze, T. Schnier, K. Meerholz and F. Würthner, *Adv. Funct. Mater.*, 2014, **24**, 4645–4653.
9. H. Shang, H. Fan, Y. Liu, W. Hu, Y. Li and X. Zhan, *Adv. Mater.*, 2011, **23**, 1554-1557.
10. J.-Y. Pan, L.-J. Zuo, X.-L. Hu, W.-F. Fu, M.-R. Chen, L. Fu, X. Gu, H.-Q. Shi, M.-M. Shi, H.-Y. Li and H.-Z. Chen, *ACS Appl. Mater. Interfaces*, 2013, **5**, 972-980.
11. J. Min, Y. N. Luponosov, A. Gerl, M. S. Polinskaya, S. M. Peregudova, P. V. Dmitryakov, A. V. Bakirov, M. A. Shcherbina, S. N. Chvalun, S. Grigorian, N. Kaush-Busies, S. A. Ponomarenko, T. Ameri and C. J. Brabec, *Adv. Energy Mater.*, 2014, **4**, 1301234.
12. J. Min, Y. N. Luponosov, D. Baran, S. N. Chvalun, M. A. Shcherbina, A. V. Bakirov, P. V. Dmitryakov, S. M. Peregudova, N. Kausch-Busies, S. A. Ponomarenko, T. Ameri and C. J. Brabec, *J. Mater. Chem. A*, 2014, **2**, 16135-16147.
13. Y. Zhang, X. Bao, M. Xiao, H. Tan, Q. Tao, Y. Wang, Y. Liu, R. Yang and W. Zhu, *J. Mater. Chem. A*, 2015, **3**, 886-893.
14. J. Mei, K. R. Graham, R. Stalder, S. P. Tiwari, H. Cheun, J. Shim, M. Yoshio, C. Nuckolls, B. Kippelen, R. K. Castellano and J. R. Reynolds, *Chem. Mater.*, 2011, **23**, 2285-2288.
15. W. Shin, T. Yasuda, G. Watanabe, Y. S. Yang and C. Adachi, *Chem. Mater.*, 2013, **25**, 2549–2556.
16. J. Liu, B. Walker, A. Tamayo, Y. Zhang and T.-Q. Nguyen, *Adv. Funct. Mater.*, 2013, **23**, 47–56.
17. V. S. Gevaerts, E. M. Herzig, M. Kirkus, K. H. Hendriks, M. M. Wienk, J. Perlich, P. Müller-Buschbaum and R. A. J. Janssen, *Chem. Mater.*, 2013, **26**, 916–926.
18. Y. Sun, G. C. Welch, W. L. Leong, C. J. Takacs, G. C. Bazan and A. J. Heeger, *Nat. Mater.*, 2012, **11**, 44–48.
19. D. H. Wang, A. K. K. Kyaw, V. Gupta, G. C. Bazan and A. J. Heeger, *Adv. Energy Mater.*, 2013, **3**, 1161–1165.
20. Y. N. Luponosov, J. Min, T. Ameri, C. J. Brabec and S. A. Ponomarenko, *Org. Electron.*, 2014, **15**, 3800–3804.
21. C. D. Wessendorf, G. L. Schulz, A. Mishra, P. Kar, I. Ata, M. Weidelener, M. Urdanpilleta, J. Hanisch, E. Mena-Osteritz, M. Lindén, E. Ahlswede and P. Bäuerle, *Adv. Energy Mater.*, 2014, **4**, 1400266.
22. B. H. Wunsch, M. Rumi, N. R. Tummala, C. Risko, D.-Y. Kang, K. X. Steirer, J. Gantz, M. Said, N. R. Armstrong, J.-L. Bredas, D. Bucknall and S. R. Marder, *J. Mater. Chem. C*, 2013, **1**, 5250-5260.
23. J. Zhou, X. Wan, Y. Liu, Y. Zuo, Z. Li, G. He, G. Long, W. Ni, C. Li, X.-C. Su and Y. Chen, *J. Am. Chem. Soc.*, 2012, **134**, 16345–16351.
24. J. Zhou, Y. Zuo, X. Wan, G. Long, Q. Zhang, W. Ni, Y. Liu, Z. Li, G. He, C. Li, B. Kan, M. Li and Y. Chen, *J. Am. Chem. Soc.*, 2013, **135**, 8484–8487.
25. Y. Lin, Y. Li and X. Zhan, *Chem. Soc. Rev.*, 2012, **41**, 4245-4272.
26. V. Malytskyi, J.-J. Simon, L. Patrone and J.-M. Raimundo, *RSC Adv.*, 2015, **5**, 354-397.
27. T. Xu and L. Yu, *Mater. Today*, 2014, **17**, 11–15.
28. Y. Li, *Acc. Chem. Res.*, 2012, **45**, 723–733.
29. C. Duan, F. Huang and Y. Cao, *J. Mater. Chem.*, 2012, **22**, 10416-10434.
30. J. Roncali, *Acc. Chem. Res.*, 2009, **42**, 1719–1730.
31. A. W. Hains, Z. Liang, M. A. Woodhouse and B. A. Gregg, *Chem. Rev.*, 2010, **110**, 6689-6735.
32. B. Walker, C. Kim and T.-Q. Nguyen, *Chem. Mater.*, 2011, **23**, 470-482.
33. V. Gupta, A. K. K. Kyaw, D. H. Wang, S. Chand, G. C. Bazan and A. J. Heeger, *Sci. Rep.*, 2013, **3**, 1965 doi: 1910.1038/srep01965.
34. Q. Zhang, B. Kan, F. Liu, G. Long, X. Wan, X. Chen, Y. Zuo, W. Ni, H. Zhang, M. Li, Z. Hu, F. Huang, Y. Cao, Z. Liang, M. Zhang, T. P. Russell and Y. Chen, *Nat. Photon.*, 2014, **9**, 35–41.

35. K. Sun, Z. Xiao, S. Lu, W. Zajaczkowski, W. Pisula, E. Hanssen, J. M. White, R. M. Williamson, J. Subbiah, J. Ouyang, A. B. Holmes, W. W. H. Wong and D. J. Jones, *Nat. Commun.*, 2015, **6**, 6013.
36. B. Kan, Q. Zhang, M. Li, X. Wan, W. Ni, G. Long, Y. Wang, X. Yang, H. Feng and Y. Chen, *J. Am. Chem. Soc.*, 2014, **136**, 15529–15532.
37. A. K. K. Kyaw, D. H. Wang, D. Wynands, J. Zhang, T.-Q. Nguyen, G. C. Bazan and A. J. Heeger, *Nano Lett.*, 2013, **13**, 3796-3801.
38. X. Liu, Y. Sun, L. A. Perez, W. Wen, M. F. Toney, A. J. Heeger and G. C. Bazan, *J. Am. Chem. Soc.*, 2012, **134**, 20609–20612.
39. Y. Liu, Y. Yang, C.-C. Chen, Q. Chen, L. Dou, Z. Hong, G. Li and Y. Yang, *Adv. Mater.*, 2013, **25**, 4657–4662.
40. Y. J. Kim, J. Y. Baek, J.-j. Ha, D. S. Chung, S.-K. Kwon, C. E. Park and Y.-H. Kim, *J. Mater. Chem. C*, 2014, **2**, 4937-4946.
41. B. Walker, A. Tamayo, D. T. Duong, X.-D. Dang, C. Kim, J. Granstrom and T.-Q. Nguyen, *Adv. Energy Mater.*, 2011, **1**, 221-229.
42. W. L. Leong, G. C. Welch, J. Seifter, J. H. Seo, G. C. Bazan and A. J. Heeger, *Adv. Energy Mater.*, 2013, **3**, 356–363.
43. Q. Shi, P. Cheng, Y. Li and X. Zhan, *Adv. Energy Mater.*, 2012, **2**, 63–67.
44. Y. Zuo, W. Ni, Q. Zhang, M. Li, B. Kan, X. Wan and Y. Chen, *J. Mater. Chem. C*, 2014, **2**, 7247-7255.
45. G. Wei, X. Xiao, S. Wang, J. D. Zimmerman, K. Sun, V. V. Diev, M. E. Thompson and S. R. Forrest, *Nano Lett.*, 2011, **11**, 4261–4264.
46. G. Wei, S. Wang, K. Sun, M. E. Thompson and S. R. Forrest, *Adv. Energy Mater.*, 2011, **1**, 184-187.
47. Y. Zhao, Z. Xie, Y. Qu, Y. Geng and L. Wang, *Appl. Phys. Lett.*, 2007, **90**, 043504.
48. M. T. Lloyd, A. C. Mayer, S. Subramanian, D. A. Mourey, D. J. Herman, A. V. Bapat, J. E. Anthony and G. G. Malliaras, *J. Am. Chem. Soc.*, 2007, **129**, 9144-9149.
49. H. Tang, G. Lu, L. Li, J. Li, Y. Wang and X. Yang, *J. Mater. Chem.*, 2010, **20**, 683-688.
50. K. Sun, Z. Xiao, E. Hanssen, M. F. G. Klein, H. H. Dam, M. Pfaff, D. Gerthsen, W. W. H. Wong and D. J. Jones, *J. Mater. Chem. A*, 2014, **2**, 9048-9054.
51. H.-Y. Chen, H. Yang, G. Yang, S. Sista, R. Zadoyan, G. Li and Y. Yang, *J. Phys. Chem. C*, 2009, **113**, 7946–7953.
52. T. S. van der Poll, J. A. Love, T.-Q. Nguyen and G. C. Bazan, *Adv. Mater.*, 2012, **24**, 3646–3649.
53. J. K. Park, C. Kim, B. Walker, T.-Q. Nguyen and J. H. Seo, *RSC Adv.*, 2012, **2**, 2232-2234.
54. H. Wang, F. Liu, L. Bu, J. Gao, C. Wang, W. Wei and T. P. Russell, *Adv. Mater.*, 2013, **25**, 6519–6525.
55. J. A. Love, S. D. Collins, I. Nagao, S. Mukherjee, H. Ade, G. C. Bazan and T.-Q. Nguyen, *Adv. Mater.*, 2014, **26**, 7308–7316.
56. (*a*) R. N. Adams, *Electrochemistry at Solid Electrodes*, Marcel Dekker: New York, 1969; (b) R. S. Nicholson, *Anal. Chem.*, 1966, **38**, 1406-1406; (*c*) R. S. Nicholson and I. Shain, *Anal. Chem.*, 1964, **36**, 706-723.
57. M. C. Scharber, M. Koppe, J. Gao, F. Cordella, M. A. Loi, P. Denk, M. Morana, H.-J. Egelhaaf, K. Forberich, G. Dennler, R. Gaudiana, D. Waller, Z. Zhu, X. Shi and C. J. Brabec, *Adv. Mater.*, 2009, **22**, 367-370.
58. H.-Y. Chen, J. Hou, A. E. Hayden, H. Yang, K. N. Houk and Y. Yang, *Adv. Mater.*, 2010, **22**, 371-375.
59. K. Schulze, M. Riede, E. Brier, E. Reinold, P. Bäuerle and K. Leo, *J. Appl. Phys.*, 2008, **104**, 074511.
60. N. Blouin, A. Michaud and M. Leclerc, *Adv. Mater.*, 2007, **19**, 2295-2300.
61. U. Asawapirom, R. Güntner, M. Forster, T. Farrell and U. Scherf, *Synthesis*, 2002, **9**, 1136-1142.
62. M. Löbert, A. Mishra, C. Uhrich, M. Pfeiffer and P. Bäuerle, *J. Mater. Chem. C*, 2014, **2**, 4879-4892.
63. J. Hou, H.-Y. Chen, S. Zhang, G. Li and Y. Yang, *J. Am. Chem. Soc.*, 2008, **130**, 16144-16145.

64. M. Weidelener, C. D. Wessendorf, J. Hanisch, E. Ahlswede, G. Götz, M. Lindén, G. Schulz, E. Mena-Osteritz, A. Mishra and P. Bäuerle, *Chem. Commun.*, 2013, **49**, 10865-10867.
65. I. Horcas, R. Fernández, J. M. Gómez-Rodríguez, J. Colchero, J. Gómez-Herrero and A. M. Baro, *Rev. Sci. Instrum.*, 2007, **78**, 013705.
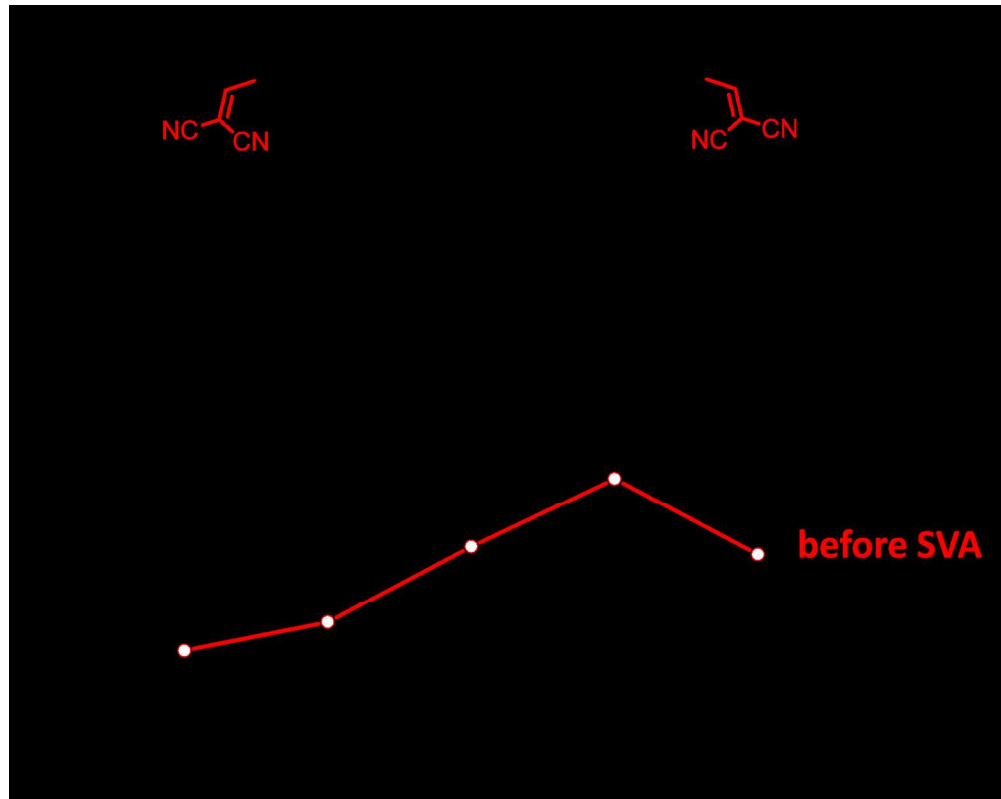
278x220mm (150 x 150 DPI)

Table of Content
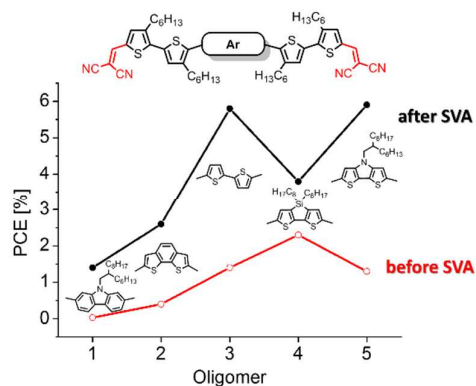
A series of dicyanovinylene-substituted A-D-A oligothiophenes comprising conjugated cores of varying donor strength were developed for applications in solution-processable organic solar cells showing significant enhancement in power conversion efficiencies upon solvent vapor annealing.